Two-scale analysis of a tight gas sandstone

Yang Song, Catherine A. Davy, Kim Thang Nguyen, David Troadec, Grégory Hauss, Laurent Jeannin, Pierre M. Adler

Two-scale analysis of a tight gas sandstone

Yang Song,[1] C. A. Davy,[1] Thang Nguyen Kim,[2] D. Troadec,[3] G. Hauss,[4] L. Jeannin,[4] and P. M. Adler[2]
[1]*Ecole Centrale de Lille, Cité Scientifique, CS20048, and LML FRE CNRS 3723, 59651 Villeneuve d'Ascq Cedex, France*
[2]*Université Pierre et Marie Curie, Laboratoire Metis, Paris, France*
[3]*IEMN, UMR CNRS 8520, BP 60069, 59652 Villeneuve d'Ascq Cedex, France*
[4]*GDF SUEZ E&P International SA, 1 place Samuel de Champlain, 92930 Paris La Défense Cedex, France*
(Received 14 January 2016; published 24 October 2016)

Tight gas sandstones are low porosity media, with a very small permeability (i.e., below 1 mD). Their porosity is below 10%, and it is mainly composed of fine noncemented microcracks, which are present between neighboring quartz grains. While empirical models of permeability are available, their predictions, which do not compare well with macroscopic measurements, are not reliable to assess gas well productivity. The purpose of this work is to compare the permeability measured on centimetric plugs to predictions based on pore structure data. Two macroscopic measurements are performed, namely dry gas permeability and mercury intrusion porosimetry (MIP), together with a series of local measurements including focused ion beam and scanning electron microscopy (FIB-SEM), x-ray computed microtomography (CMT), and standard two-dimensional (2D) SEM. Numerical modeling is performed by combining analyses on two scales, namely the microcrack network scale (given by 2D SEM) and the individual 3D microcrack scale (given by either FIB-SEM or CMT). The network permeability is calculated by means of techniques developed for fracture networks. This permeability is proportional to the microcrack transmissivity, which is determined by solving the Stokes equation in the microcracks measured by FIB-SEM or CMT. Good correlation with experimental permeability values is only found when using transmissivity from 3D CMT data.

DOI: 10.1103/PhysRevE.94.043316

I. INTRODUCTION

Tight gas reservoirs have specific petrophysical properties, which may hinder proper gas recovery [1]. They have a low absolute permeability (below 0.1 mD, i.e., $<10^{-16}$ m^2) and a connected porosity smaller than 10%. While empirical permeability models are available [2–5], they necessitate a delicate fitting of their parameters, and their predictions are not consistent with actual laboratory measurements [6]. A better understanding of the relevant scale(s) controlling fluid transport would help improve permeability prediction and gas well production rates.

Low permeability sandstones are mainly made of SiO_2 grains, which have a typical size of several hundreds of μm [7]. SiO_2 grains are separated by a network of partially cemented fine microcracks, with sizes typically ranging between several μm down to several tens of nm. These microcracks are linked to individual bigger pores, often partially filled with illite-type clay, yet of a relatively limited volume. The structure of tight sandstones can be schematized by polyhedra, which are separated by plane and permeable polygonal microcracks. It should be emphasized that the term pore space, which is used for the sake of brevity, refers to this microcrack network.

Owing to the wide size distribution of the microcrack apertures, low permeability sandstones, like many low permeability materials, are composed of several pore structures of various scales, which are superposed on one another [8]. Presently, it is impossible to measure the pore geometry relevant for fluid transport in one step with a unique experimental device since the ratio between the largest and the smallest relevant scales is too large. The same is true for the very same reason for the numerical determination of permeability. Therefore, it is necessary to proceed in several steps which combine the pore structure properties by homogenization techniques [9].

In this paper, the geometry of the individual microcracks is determined by focused ion beam and scanning electron microscopy (FIB-SEM) for the smallest and x-ray computed microtomography (CMT) for the widest, while cross sections of the sandstone pore network are digitized from two-dimensional (2D) SEM measurements, over several mm^2 surface areas. In other words, FIB-SEM and CMT provide the transversal structure of the microcracks, while the statistical characteristics of the microcrack network are given by SEM. For comparison purposes, classical macroscopic measurements such as permeability and mercury injection porosimetry (MIP) are performed. All experimental measurements at the macroscopic scale (dry gas permeability, MIP) and at the microscopic scale (FIB-SEM, CMT, and 2D SEM imaging) are presented in Sec. II.

Then, a methodology is proposed to derive the permeability of a given tight sandstone. It is based on measurements of the pore structure on two different scales. First, the transmissivity of some individual microcracks (measured either by FIB-SEM or by CMT) is obtained by solving the Stokes equation in these structures with adequate boundary conditions. Second, the microcrack network is assimilated to a fracture network to which the methodology presented in [10] is applied, the statistical properties of this network are measured on the 2D SEM images, and the dimensionless macroscopic permeability of the fracture network is derived by using a semiempirical relation derived by [11]. These two relations are combined to yield the dimensional macroscopic sandstone permeability.

In Sec. III, the density of microcracks is estimated from trace maps of the pore network (from 2D SEM imaging), by three different means based on the number of intersections with scan lines, on the surface density of microcracks and on the intersections between microcracks per unit surface. Then, a general formula derived from systematic numerical

computations [10] is used to deduce the macroscopic dimensionless permeability K, which is proportional to the fracture transmissivity σ.

In Sec. IV, the transmissivity σ is evaluated at the scale of the individual microcracks given by FIB-SEM and CMT. The analysis is performed by FIB-SEM down to 35.5 nm in order to get a complete picture of the porosity, even on the smallest length scales which are not *a priori* relevant for permeability, but which can be important for other transports such as convection and diffusion. A single-phase lattice Boltzmann code is used; according to the standard terminology, it is a D3Q19 code with two relaxation times, and the classical bounce-back condition is used at the solid interface. Each sample is completed by its mirror image in order to avoid overall boundary effects. More details are given by [12].

Then, the macroscopic permeability is predicted and discussed in Sec. V. The material is assumed isotropic, in good agreement with macroscopic dry gas permeability measurements and 2D SEM measurements of fracture density. The numerical results are compared to the experimental data. A discussion follows together with possible extensions of the present study.

Concluding remarks are given in Sec. VI.

II. EXPERIMENTAL STUDY: PERMEABILITY AND PORE STRUCTURE

All experiments in this contribution are performed by using a single sandstone sample (reference no. T-2390-82). It is a plug of diameter 37 mm and of length 34.65 mm (Fig. 1).

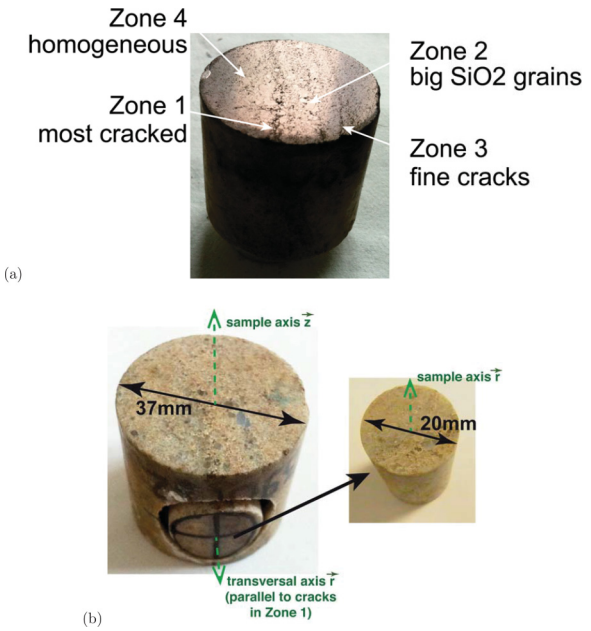

FIG. 1. The tight sandstone sample T-2390-82. (a) Definition of the four zones on the upper surface where 2D SEM imaging is performed. (b) Samples for macroscopic gas permeability measurements. Dry gas permeability K_{gas} is measured along the vertical z axis prior to transversal overcoring along the radial r axis (parallel to the biggest cracks in zone 1) to a diameter of 20 mm The permeability of the smaller 20mm diameter sample is also along the r axis.

Previous poro-mechanical experiments have been performed on this sample. They are reported in [7].

A. Macroscopic dry gas permeability

Details of the experimental methodology are given in [7] and [13]. The sample is oven-dried at 105 °C until mass stabilization. In [7], this sample was tested in the same dry state, under a hydrostatic stress (i.e., confining pressure P_c) ranging from 5 to 45 MPa along the z axis (Fig. 1). Its gas permeability at $P_c = 5$ MPa is equal to 2.0×10^{-17} m^2 (0.02 mD).

In this study, a hydrostatic stress $P_c = 5$ MPa is imposed on the sample. A smaller gas permeability K_{gas} of 0.97×10^{-17} m^2 (0.0097 mD) is measured, due to the effect of the previous hydrostatic stress cycle up to 45 MPa (associated with irreversible microcrack closure).

To check sample isotropy for fluid transport, a radial overcoring along the r axis to a cylinder of 20 mm diameter was performed [Fig. 1(b)]; this direction was chosen to be parallel to the largest cracks, which can be observed on the upper face of the full sample in Fig. 1(a). The corresponding dry gas permeability K_{gas} of the T-2390-82 sandstone remains within the range measured along the z axis. At $P_c = 5$ MPa, K_{gas} is equal to 1.3×10^{-17} m^2 (0.013 mD), which is only 1.3 times more than along z at the same P_c.

In order to validate the numerical predictions, a value for K_{gas} equal to $1.4 \pm 0.5\times10^{-17}$ m^2 (0.014 ± 0.005 mD) is retained in the following; it corresponds to a hydrostatic stress $P_c = 5$ MPa.

B. Indirect characterization of the pore structure

1. *Macroscopic water porosity*

The water porosity of sample T-2390-82 (with a diameter of 37 mm) is equal to 3.26% [7]. For the overcored T-2390-82 sample of 20 mm diameter [Fig. 1(b)], a porosity of 2.75% is obtained after water saturation, followed by drying at 105 °C until mass stabilization. This limited porosity decrease (from 3.26% to 2.75%) is attributed to the heterogeneity of the sample, since it remains of centimetric size after overcoring. Therefore, it is still assumed to be representative of the macroscopic pore structure.

2. *Nitrogen adsorption and MIP.*

Nitrogen adsorption is performed with a MICROMERITICS ASAP 2010 apparatus on a sandstone chip of a few cm^3. This method characterizes indirectly pores of diameters d up to 140 nm; the proportion of so-called micropores ($d < 2$ nm diameter) is determined, when compared to mesopores (2–50 nm) and macropores ($d > 50$ nm), as defined by IUPAC (International Union of Pure and Applied Chemistry) classification [14]. As shown in Fig. 2(a), the volume of micropores, corresponding to relative pressures below 0.1, is very limited, and represents 1.8% of the total adsorbed volume. Most of the adsorption occurs for relative pressures above 75%, i.e., for pores of diameter greater than 7.5 nm. This means that the T-2390-82 sandstone is mainly composed of mesopores and macropores; their proportion is usually determined by mercury intrusion porosimetry (MIP) [15].

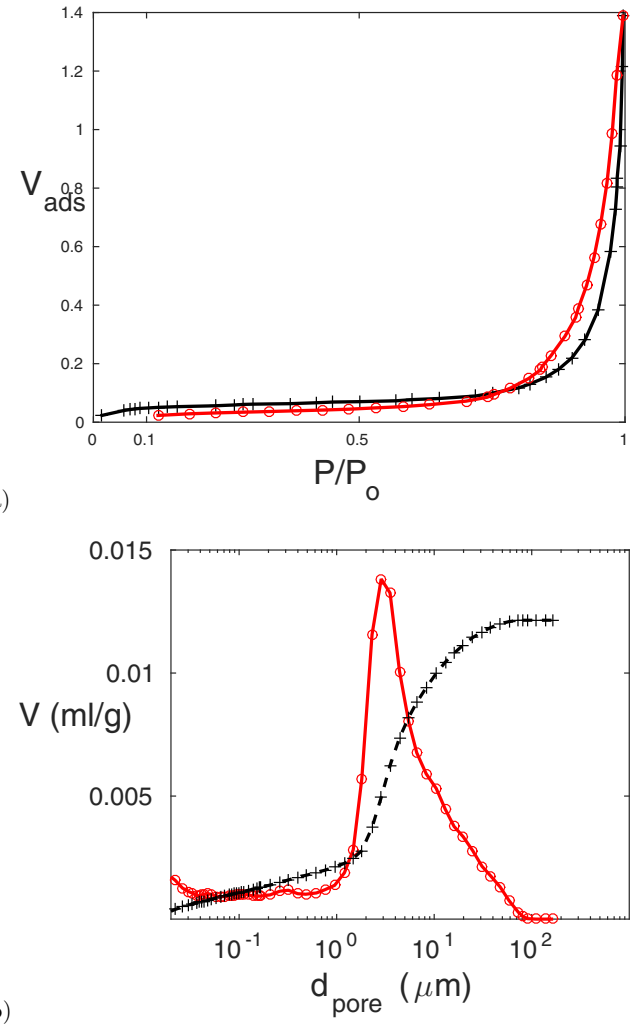

FIG. 2. Indirect PSD results for T-2390-82 sandstone. (a) Nitrogen adsorption as a function of the relative pressure P/P_o. Data are for adsorption (black solid line, +), desorption (red broken line, ○). (b) Mercury intrusion porosimetry (MIP) results (plotted after blank cell and conformance corrections [15]). Data are for intrusion (red solid line, ○), cumulated intrusion (black broken line, +).

MIP is performed using a MICROMERITICS AutoPore IV 9500 up to 200 MPa, which corresponds to intruded pores down to 4 nm. The mercury contact angle is equal to 130°. All pore size distribution curves are plotted after blank cell and conformance corrections [15]. Results [Fig. 2(b)] show a characteristic pore size of about 350 nm, with a limited contribution of pores between 1 and 10 μm to the cumulative pore size distribution. The use of FIB-SEM imaging (with voxel sizes down to 10–20 nm [8]) is justified by the value of this peak pore size. Moreover, following [6], MIP provides parameter values for the empirical permeability correlations of [2] to [5].

For the Swanson model, the intruded pore volume V_b and pressure P_c are determined at the apex of the MIP curve at respectively 27.06% and 517.5 psi; hence, the predicted permeability is equal to 0.95 mD (i.e. 9.5×10^{-16} m^2).

For the Thomeer model, it is assumed that the mercury pore volume at the end of intrusion is 100%, which implies that $P_d = 9.82$ psi and $G = 0.82$ when fitting on the linear part of the $[1/\log_{10}(V_b), \log_{10}(P_c)]$ curve (i.e., between 0% and 6% intruded pore volume). This yields a permeability of 0.5 mD (i.e., 5.0×10^{-16} m^2).

For the Kamath model, the Brooks-Corey fitting is performed with an assumption of zero residual saturation $S_r = 0$ and on a proportion of mercury intrusion ranging between 20% and 60% (linear portion of the MIP curve); thus, the identified parameters are $\lambda = 0.5025$ and $\log_{10}(P_e) = 4.1604$. The predicted permeability is equal to 9.3×10^{-3} mD (i.e., 0.093×10^{-16} m^2).

It is concluded that the three empirical models provide significantly different permeability values. However, the Swanson and Thomeer models predict the same order of magnitude of 0.1 mD, which is one order of magnitude greater than our experimental data for a centimetric plug (0.014 mD, Sec. II A). The Kamath model provides the closest prediction to experimental data with a value of 0.0093 mD; this is smaller than our experimental data by a factor of 1.5. The empirical models also require varying assumptions to use the MIP curve, and choosing the adequate one is not obvious. These elements justify the present research.

C. Direct measurement of the pore structure

1. Bidimensional (2D) SEM

Scanning electron microscopy (SEM) observations are performed on a SEM Hitachi S3600N apparatus, with secondary electron (SE) and backscattered electron (BSE) detectors. BSE images may be coupled to energy dispersive spectroscopy (EDS) for chemical element analysis.

Macrophotographs of the polished sample surface show different porous zones corresponding to varying pore densities [Fig. 1(a)]. Several tens of images, spanning several mm, have been recorded; they correspond to the various zones indicated in Fig. 1(a).

As a feasibility step, only two images have been selected for quantification; the first one is located in the highly porous zone 1, and the second one in the homogeneous zone 4. BSE images show the presence of SiO_2 grains, directly and partially cemented along intergranular microcracks, and a few inclusions of iron and magnesium oxides [Fig. 3(c)]. Upon increasing the SEM magnification, the thickness of intergranular microcracks is seen to be highly variable, from several tens of nm [less than 50 nm in Fig. 4(a)] to a few μm [Fig. 4(b)]. This justifies the use of both FIB-SEM (for the narrowest microcracks) and CMT (for the widest microcracks) to characterize the 3D microcrack volumes.

After 2D SEM imaging, two types of processing are performed on the 2D grayscale images, in order to characterize the pore network. First, the trace of the joints between the individual SiO_2 grains is detected manually (with tracing tools in Adobe Photoshop software), and the image is binarized for further processing (joint density, etc.) [see Figs. 3(b) and 3(d)]. Second, each image is processed by each of the seventeen threshold algorithms available. Each algorithm yields an evaluation of the porosity; only the algorithms which yield a realistic value are retained. In most cases, several algorithms yield the correct porosity. Additional details can be found in [8,16] and in Appendix 2.

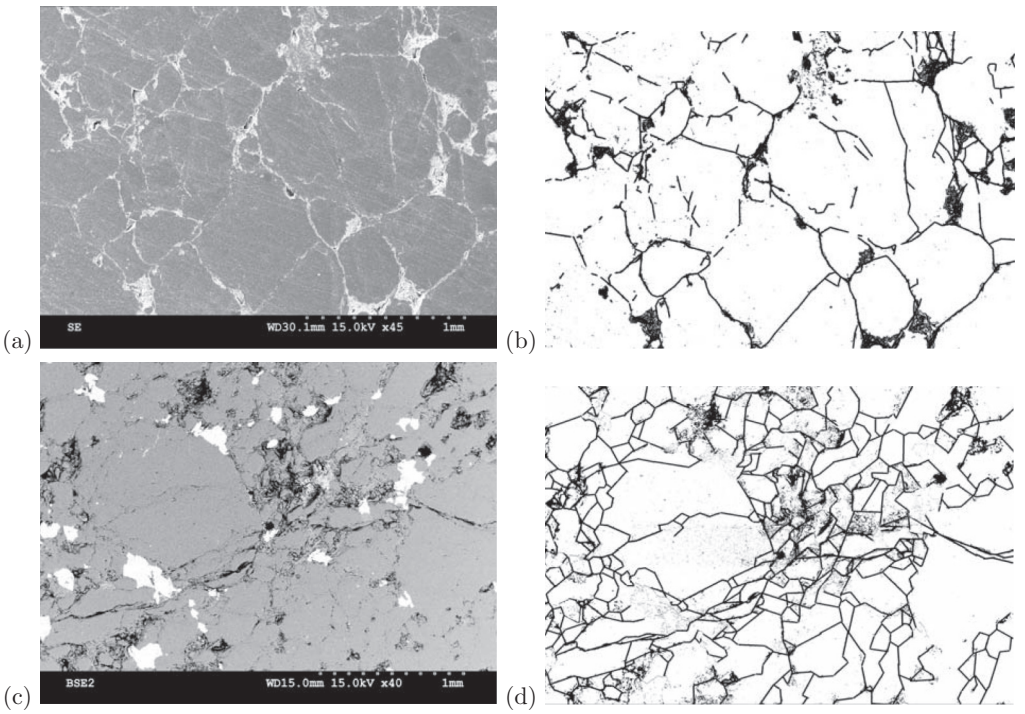

FIG. 3. Two dimensional SEM measurements of T-2390-82 sandstone. (a) SEM1 is located in the homogeneous zone 4, and observed with the SE detector (microcracks appear light grey); the corresponding trace map is given in (b). (c) SEM2 is from the most porous and cracked zone 1, and it is observed with the BSE detector (microcracks appear black); it is interpreted as a trace map in (d).

2. *X-ray computed microtomography (CMT)*

Several series of 1100–1260 images (1577 × 1112 pixels^2) were acquired and processed by x-ray computed microtomography (CMT) [17,18] at the Isis 4D platform (Lille, France). Details on the methodology providing the images and their segmented pore areas are given in Appendix 1.

Subsamples of T-2390-82 are imaged with decreasing voxel size, i.e., with decreasing overall size. First, Fig. 5 (left) displays the overcored subsample of 20 mm diameter and 35 mm height, tested for dry gas permeability, with a voxel size of 13 μm and the 3D rendering of its segmented pore volume. Second, a parallelepipedic sample with a 5 mm width is given in Fig. 5 (middle) with its 3D pore volume. Third, Fig. 5 (right) shows a thin rod of 0.946 mm × 0.667 mm sectional area, with a voxel size of 0.6 μm (i.e., 600 nm) and its 3D pore volume.

From the binary images extracted from CMT also, the 2D and 3D continuous pore size distributions (CPSDs) are determined as described by [19]. For all three samples, results of 2D and 3D CPSDs are close and provide a unimodal distribution. For the thin rod (600 nm voxel size), the peak pore size is centered on 4 μm; it is 18 μm for a 4.37 μm voxel size, and 52.4 μm for a 13 μm voxel size.

3. *FIB-SEM*

FIB-SEM analysis provides 3D images of the microstructure, without any preliminary preparation (and damage) of the observed surface, at small length scales of several tens of nm. Even if these lengths scales are likely not relevant for permeability, it is interesting to have a complete view of the porosity inside the medium under study, and to quantify their contribution. Methodological details are given in Appendix 2.

The sample obtained on T-2390-82 has a voxel size of $48.8\times35.71\times50.0$ nm^3, and a total investigated volume of $9.874\times2.007\times15$ μm^3 [Fig. 6(a)].

The 3D pore network is obtained from the raw FIB-SEM image stack, by filtering and segmentation of each individual image using IMAGEJ software. Details on the methodology providing the images and their segmented pore areas are given in Appendix 2. The 3D object (pore volume) is generated by using AMIRA (FEI) software, and a continuous pore size distribution (CPSD) is obtained from the 3D object (Fig. 7), by using the method described in [19] and applied by [20–22], as for our CMT samples. It is readily seen in Fig. 7 that the CPSD is of an almost discrete nature, with four distinct peaks at 80, 120, 180, and 240 nm; the highest peak (corresponding to the greatest relative pore volume) is at 180 nm. These peaks are attributed to four distinct crack objects, with individual crack openings of 80, 120, 180, and 240 nm. The 3D pore volume is connected between the two end surfaces perpendicular to the y axis.

D. Comparison of the various pore structure observations

The various imaging techniques and the indirect methods are compared in terms of 3D pore size distributions in Fig. 7 and Table I. For voxel sizes $a = 13$ and 4.4 μm, the pore volumes of CMT samples are not connected from one surface to another, despite porosities of $1.016\% \pm 0.36$ and $1.88\% \pm 0.17$, most probably because the voxel sizes are too large.

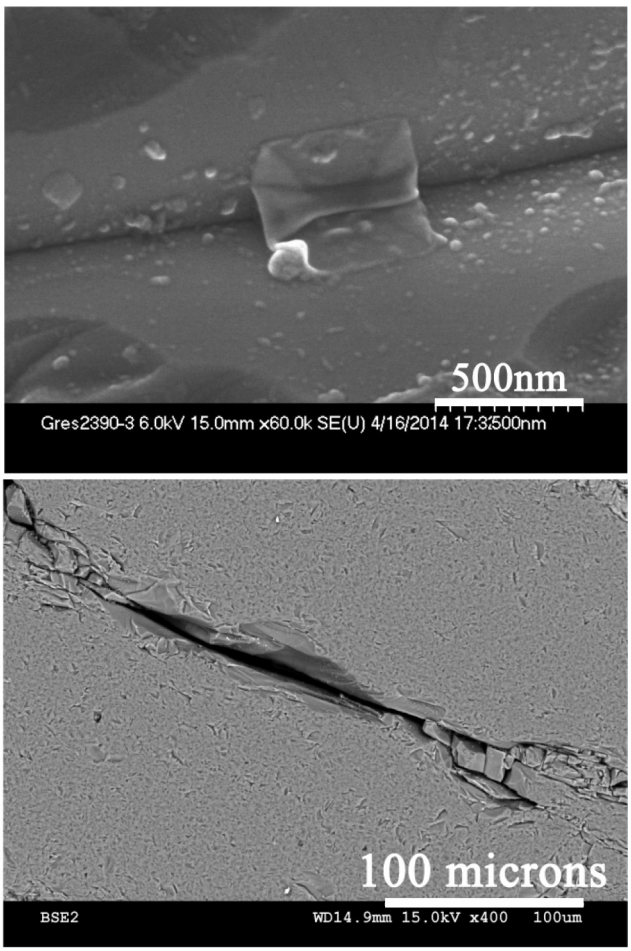

FIG. 4. 2D SEM of T-2390-82 sandstone: close-up views of single micro cracks between two quartz grains, highlighting their highly variable width, from (a) less than 50 nm and up to (b) several microns. (a) and (b) are taken from zones 4 and 1, respectively.

Compared to water porosity (2.8–3.2%), MIP provides a greater value (4.89%), possibly due to sample damage. Moreover, the CMT of the 0.8 mm rod (600 nm voxel size) provides a connected pore volume (Fig. 5) corresponding to an individual microcrack between two quartz grains, of porosity $1.34\% \pm 0.15$ and average opening of 4 μm. Although significantly smaller, the FIB-SEM sample provides a porosity of 1.27%, which is similar to CMT, and a typical opening of 180 nm (peak value of the 3D PSD); it is connected between two parallel end surfaces. Also, the FIB-SEM sample possesses a secondary pore size peak at 80 nm (Fig. 7), which is attributed to a second characteristic crack opening; it means that this 3D sample has a significant variation in its crack aperture distribution. Therefore, any prediction of permeability using simple 1D laws, e.g., Poiseuille's law, and based on these FIB-SEM data is bound to provide inaccurate results (Table II).

For permeability prediction purposes, the connected pore volumes given by the 600 nm voxel sized CMT and by FIB-SEM are the only ones to be used. At this stage, however, it is difficult to determine the respective contributions of both 3D microcracks (given by CMT and FIB-SEM) to fluid transport, namely the ones with an average opening of 180 nm (FIB-SEM) or of 4 μm (CMT).

III. PREDICTION OF PERMEABILITY ON THE MACROSCOPIC SCALE

The statistical characteristics of the fracture network are derived from the trace maps of the microcrack (or fracture) networks, which are displayed in Fig. 3. The reader is referred to [10] and [11] for a complete presentation of the methodology.

A. Theoretical background

The images (Fig. 3) are used to count the items that they contain, such as the number of intersections of the traces with scan lines per unit length $\langle n_I \rangle$, the number of traces per unit surface Σ_t, and the number of intersections between fractures per unit surface Σ_p. If the fractures are assumed to be convex, uniformly distributed in space, and isotropically oriented, some general relations are obtained between the observed quantities $\langle n_I \rangle, \Sigma_t, \Sigma_p$ and the fracture density ρ, the average fracture area $\langle A \rangle$, and perimeter $\langle P \rangle$. These relations are expressed as (cf. [10])

$$\langle n_I \rangle = \frac{1}{2}\rho\langle A \rangle, \quad \Sigma_t = \frac{1}{4}\rho\langle P \rangle, \quad \Sigma_p = \frac{\pi}{16}\rho^2\langle A \rangle^2. \tag{1}$$

However, in most cases, these relations need a hypothesis on the fracture shape, or at least on a shape factor. Here, the simplest assumption is made; i.e., the fractures are assumed circular and of the same radius R. An order of magnitude of R is obtained from the trace maps. Therefore, the images provide three estimations ρ_n, ρ_t, and ρ_p of the fracture density, as

$$\rho_n = \frac{2\langle n_I \rangle}{\pi R^2}, \quad \rho_t = \frac{2\Sigma_t}{\pi R}, \quad \rho_p = \frac{4}{\pi R^2}\left(\frac{\Sigma_p}{\pi}\right)^{1/2}. \tag{2}$$

This way of using the data from trace maps is the simplest one. More sophisticated ways can be used, but they require more information on the pore network structure.

However, the average trace length, which is observed on a trace map, is not equal to $2R$. It can be shown that, under the same hypotheses as previously, the average trace length is equal to $R\pi/2$ (cf. [9]). Since this quantity is only estimated and not precisely measured in this study, this additional factor is not taken into account and $2R$ is retained.

Then, one derives the dimensionless density ρ', which is defined as the average number of intersections for a fracture in the network. For circular fractures, it is expressed as

$$\rho' = \pi^2 R^3 \rho. \tag{3}$$

This quantity is shown to control the percolation properties of the pore network [10]; the dimensionless percolation threshold ρ'_c is close to 2.3, whatever the fracture shape. ρ' also provides a prediction for the network permeability K_n or its dimensionless value K'_n as

$$K'_n = \frac{K_n R}{\sigma} = \frac{\alpha_K \, \Delta\rho'^2}{1 + \beta_K \Delta\rho'}, \tag{4a}$$

with

$$\Delta\rho' = \rho' - \rho'_c, \quad \alpha_K = 0.037, \quad \beta_K = 0.155, \tag{4b}$$

where σ is the fracture transmissivity. Let us now apply these concepts to the trace maps of our 2D SEM images (Fig. 3).

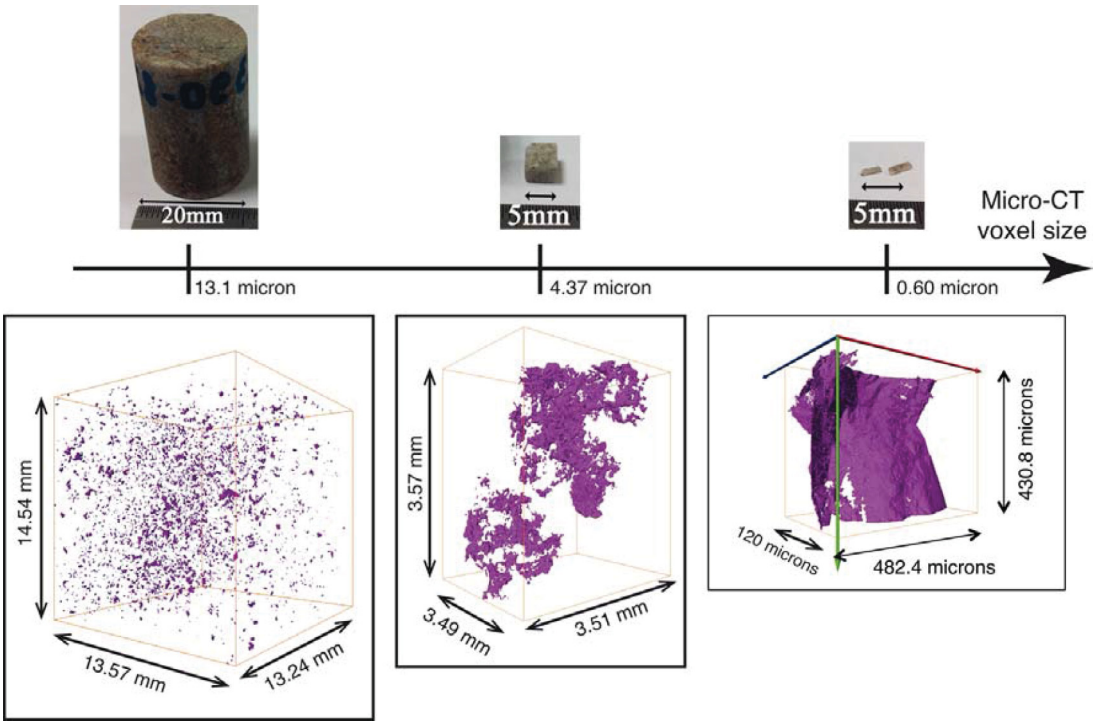

FIG. 5. Three different micro-CT samples of T-2390-82 sandstone: (upper left) 20 mm diameter and (lower left) its 3D nonconnected pore volume rendering; (upper middle) 5 mm wide parallelepipedic sample and (lower middle) its 3D nonconnected pore volume rendering; (upper right) 0.9 mm section rod and (lower right) its 3D connected pore volume rendering.

B. Trace map SEM1

Image SEM1 [Figs. 3(a) and 3(b)] is taken in the homogeneous zone 4 of sample T-2390-82 (Fig. 1). The size of SEM1 is 2560×1731 pixels; 1 mm corresponds to 446 pixels. It is a good starting point, since it is relatively small and its structure is relatively simple.

This picture is printed on an A4 sheet and the dimensionless density is derived using the measurements made on this sheet without going back to the real dimensions of the picture, as will be shown. For the sake of completeness, the actual dimensions and densities are often given in brackets.

First, the number of traces is counted. This process includes some arbitrariness in the choice of the linear elements as individual traces. However, only the order of magnitude is important. As seen in Fig. 3(b), 55 fractures are identified on a surface of 20×28.7 cm^2, which is a little smaller than the A4 format.

Second, two horizontal and three vertical scanlines are drawn on the trace map. The two horizontal scan lines cross

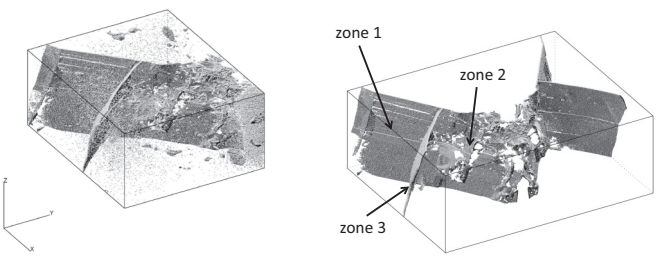

(a) (b)

FIG. 6. The initial FIB-SEM pore volume sample for T-2390-82 sandstone in (a) with 674×562×300 parallelipipedic voxels of size 48.8×35.71×50 nm^3. In (b), the percolating component is retained along the y axis with cubic voxels of size 48.8 nm.

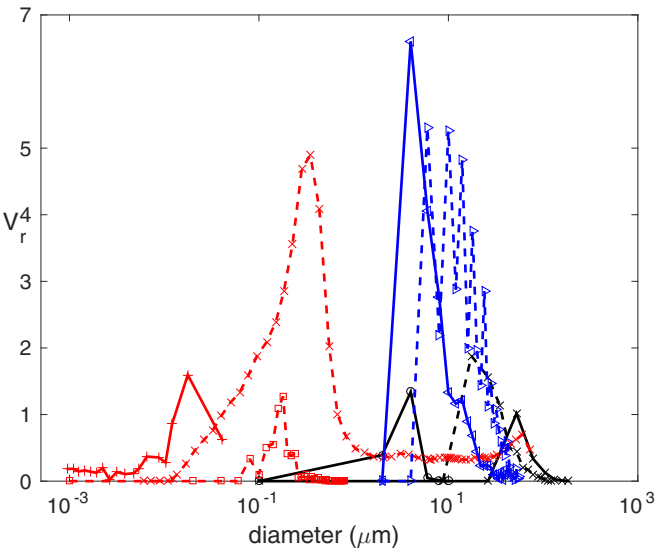

FIG. 7. The relative pore volume (in percent) obtained by different direct or indirect methods, for T-2390-82 sandstone. Data are for XRT 0.6 μm (o, black solid line), XRT 4.37 μm (×, black broken line), XRT 13.1 μm (×, black solid line), N2 adsorption (+, red solid line), MIP (1) (×, red broken line), 2D SEM medium density zone (◁, blue solid line), 2D SEM high density zone (▷, blue broken line), FIB-SEM 48.8×35.7×50 nm (□, red broken line).

TABLE I. Main characteristics of the pore structure of subsamples taken from the same T-2390-82 sandstone sample (of initial diameter 37 mm and 34.65 mm height). Water imbibition results are given for the initial 37 mm diameter sample, whereas all the columns after "Water imbibition" correspond to smaller and smaller subsamples. The porosity of the FIB-SEM sample is close to that of the 0.9 mm rod imaged by CMT. The number in parentheses corresponds to the secondary peak.

Sample name	Water imbibition	20 mm diam. CMT	MIP	5 mm wide CMT	2D SEM medium density zone	2D SEM high density zone	0.9 mm rod CMT	FIB-SEM
Sample area or volume	53.8 cm^3	2.61 cm^3	1.43 cm^3	43.7 mm^3	6 mm^2	6 mm^2	0.216 μm^3	26157 nm^3
d_{peak} (μm)		52.4	0.35 (60.3)	17.5	6	4	4	0.18
ϕ (%)	2.8–3.2	1.016 ± 0.36	4.89	1.88 ± 0.17	5.3 ± 2.2	6.6 ± 1.6	1.34 ± 0.15	1.27 ± 0.02

$9 + 7 = 16$ traces along $28.7 \times 2 = 57.4$ cm while the three vertical scan lines cross $5 + 3 + 6 = 14$ traces along $20 \times 3 = 60$ cm. Therefore, the numbers of intersections per unit length are $16/57.4 = 0.28$ and $14/60 = 0.23$ for the horizontal and the vertical scan lines, respectively. Since the two directions yield approximately the same result, the image can be said to be approximately isotropic; the number of intersections can be added to yield a single number, i.e., 30 traces along 117.4 cm.

Third, the number of intersections between fractures is estimated to be 43.

A rough estimation of the average radius R_1 for image SEM1 is 2.5 cm (i.e., 0.49 ± 0.01 mm at the actual image scale, where the variation in the length measurement corresponds to the uncertainty on the actual scale calculation). The perimeter and area of the corresponding disk are

$$P = 15.7 \text{ cm (or } 3.08 \pm 0.01 \text{ mm)},$$
$$A = 19.6 \text{ cm}^2 \text{ (or } 0.75 \pm 0.03 \text{ mm}^2\text{)}. \quad (5)$$

Therefore, according to (2), one obtains

$$\rho_n = \frac{2 \times 30}{117.4 \times 19.6} = 2.6 \times 10^{-2} \text{ fractures/cm}^3 \text{ (or } 3.5 \pm 0.2 \text{ fractures/mm}^3\text{)}, \quad (6a)$$

$$\rho_t = \frac{4 \times 55}{15.7 \times 20 \times 28.7} = 2.44 \times 10^{-2} \text{ fractures/cm}^3 \text{ (or } 3.2 \pm 0.2 \text{ fractures/mm}^3\text{)}, \quad (6b)$$

and

$$\rho_p = \frac{4}{\pi \times 20 \times 28.7} \left(\frac{51}{\pi \times 20 \times 28.7} \right)^{1/2} = 3.14 \times 10^{-2} \text{ fractures/cm}^3 \text{ (or } 4.2 \pm 0.2 \text{ fractures/mm}^3\text{)}. \quad (6c)$$

These three estimations are very close and the average value $\rho_1 = 2.7 \times 10^{-2}$ fractures/cm^3 (or 3.6 fractures/mm^3) is retained. By application of (3), the dimensionless density is

$$\rho_1' = 2.7 \times 10^{-2} \times 154 = 4.16. \quad (6d)$$

The value of ρ_1' is identical whatever the scale considered (either that of the A4 format paper or the actual scale). By application of (4a), the dimensionless permeability is

$$K_{n1}' = 9.9 \times 10^{-2}. \quad (7)$$

As for ρ_1', the value of K_{n1}' is identical, whether the calculations are performed with the A4 format scale or with the actual image scale.

TABLE II. Local transmissivities σ of FIB-SEM sample and CMT sample in m^3, as calculated from their 3D pore volume (Lattice-Boltzmann code) and compared with Poiseuille's law prediction.

Sample	a (nm)	Size (voxel)	K_{yy}'	σ (m^3)
		FIB-SEM		
Total	35.71	$680 \times 1124 \times 420$	0.66×10^{-3}	1.4×10^{-24}
Zone 1	35.71	$511 \times 512 \times 206$	9.29×10^{-3}	2.16×10^{-22}
Zone1 sech11w	35.71	$511 \times 412 \times 206$	5.25×10^{-3}	1.21×10^{-22}
Zone 2	35.71	$361 \times 410 \times 206$	0.62×10^{-3}	1.02×10^{-23}
Zone 3	35.71	$260 \times 240 \times 206$	1.16×10^{-2}	1.38×10^{-22}
Poiseuille's law ($b = 180$ nm)				4.8×10^{-22}
		CMT (rod-shaped)		
Total	600	$804 \times 1436 \times 414$	0.175×10^{-2}	1.6×10^{-19}
Portion b	600	$534 \times 576 \times 414$	0.267×10^{-2}	2.4×10^{-19}
Portion c	600	$270 \times 576 \times 414$	0.466×10^{-3}	4.2×10^{-20}
Poiseuille's law ($b = 4$ μm)				5.3×10^{-18}

A last number is still needed, which is the real value of R_1; because of the value of a pixel, one easily obtains

$$R_1 = 2.5\times\frac{1}{28.7}\times\frac{10^{-3}}{446}\times 2560 = 5\times10^{-4}\ \text{m} = 500\ \mu\text{m}. \tag{8}$$

C. Trace map SEM2

Image SEM2 is taken from the most cracked zone 1 of sample T-2390-82 [Fig. 1(a)]. It is displayed in Figs. 3(c) and 3(d) as the original grayscale image and its associated trace map. It is much denser and more comprehensive than SEM1. The size of SEM2 is 2560×1734 pixels; 1 mm corresponds to 813.5 pixels. The developments are essentially the same as in Sec. III B. Note that the analysis was performed by hand on an A3 sheet; hence, the dimensions in cm are different. The image itself is $28.3\times40.5\ \text{cm}^2$.

First, the number of traces is counted and 521 fractures are identified. Second, two horizontal and three vertical scan lines are drawn on the trace map. The two horizontal scan lines cross $23+23=46$ traces along $40.5\times2=81$ cm while the three vertical scan lines cross $19+18+13=50$ traces along $28.3\times3=84.9$ cm. Since the two directions yield again approximately the same number of intersections per unit length, the trace map is approximately isotropic and the number of intersections can be added, i.e., 96 traces along 165.9 cm.

Third, there are also 502 intersections between traces. The measurement area is $28.3\times40.5\ \text{cm}^2$.

A rough estimation of the average radius R_2 in image SEM2 is 1.5 cm (or 0.117 ± 0.01 mm). The corresponding perimeter and area are

$$\begin{aligned} P_2 &= 9.4\ \text{cm}\ (0.81\pm0.01\ \text{mm}),\\ A_2 &= 7.07\ \text{cm}^2\ (0.052\pm0.001\ \text{mm}^2). \end{aligned} \tag{9}$$

Therefore, according to (2), one obtains

$$\rho_n = \frac{2\times96}{165.9\times7.07} = 0.16\ \text{fractures/cm}^3 \quad (341\ \text{fractures/mm}^3), \tag{10a}$$

$$\rho_t = \frac{4\times521}{9.4\times28.3\times40.5} = 0.19\ \text{fractures/cm}^3 \quad (405\ \text{fractures/mm}^3), \tag{10b}$$

$$\rho_p = \frac{4}{7.07}\left(\frac{502}{\pi\times28.3\times40.5}\right)^{1/2} = 0.21\ \text{fractures/cm}^3 \quad (448\ \text{fractures/mm}^3). \tag{10c}$$

These three estimations are remarkably close and we shall take the average $\rho_2 = 0.19$ fractures/cm^3. By application of (3), the dimensionless density is

$$\rho_2' = 0.19\times33.3 = 6.33. \tag{10d}$$

By application of (4a), the dimensionless permeability is

$$K_{n2}' = 0.37. \tag{11}$$

A last number is still needed, which is the real value of R_2. Because of the value of a pixel, one easily obtains

$$R_2 = 1.5\times\frac{1}{40.5}\times\frac{10^{-3}}{813}\times2560 = 1.2\times10^{-4}\ \text{m} = 120\,\mu\text{m}, \tag{12}$$

which is a satisfactory order of magnitude.

D. Concluding remarks

This section may be ended up by two remarks.

First, for each trace map, the three estimations of ρ which are derived from (1) are very close. This implies that the assumptions (i.e., uniform distribution, isotropic orientation, and circular shape), which are made to derive these numbers, are reasonably satisfied.

Second, in dimensionless terms, the two previous estimations of permeability are not very far apart ($K_{n1}' = 9.9\times10^{-2}$ and $K_{n2}' = 37\times10^{-2}$). However, if it is assumed that the fractures have identical transmissivity σ in both cases, (4a) yields

$$K_1 = \frac{K_{n1}'}{R_1}\sigma = 198\sigma, \quad K_2 = \frac{K_{n2}'}{R_2}\sigma = 3083\sigma. \tag{13}$$

This means that the second estimation of permeability is fifteen times larger than the first one.

IV. PREDICTION OF FLUID TRANSPORT AT THE SMALL SCALE: DETERMINATION OF FRACTURE TRANSMISSIVITY

The methodology is detailed in [23]. It is based on the use of the CMT and FIB-SEM data in a way similar to [24]. The determination of the fracture transmissivity σ by solving the Stokes equation was initiated by [25].

A. General

In order to determine σ, one needs to solve the Stokes equation, which is expressed as

$$-\nabla p + \mu\nabla^2\boldsymbol{v} = 0, \tag{14a}$$

$$\nabla\cdot\boldsymbol{v} = 0, \tag{14b}$$

where p and $\boldsymbol{v}$ denote pressure and velocity, respectively; μ is the fluid viscosity.

This system should be supplemented by boundary conditions. Assuming that the solid matrix is impermeable, the fluid velocity should vanish on the two solid surfaces $S_p^{\pm}$, which limits the void space as

$$\boldsymbol{v} = 0 \quad \text{on } S_p^+,\ S_p^-,\ S_l, \text{ and } S_r. \tag{15}$$

In addition, spatially periodic boundary conditions are applied at the lateral boundaries of the sample. The driving force is a macroscopic pressure gradient $\overline{\nabla p}$ imposed on the sample.

Let Q be the flow rate generated by $\overline{\nabla p}$. For a porous medium, the easily measurable quantity is the flow rate per unit surface. However, for a fracture, this quantity is the flow rate J per unit fracture width; indeed, the width W of the fracture is easy to measure and unambiguous in a laboratory

experiment; note that the contact zones are also taken into account. The *fracture transmissivity* σ can be derived from J as

$$J = \frac{Q}{W} = -\frac{\sigma}{\mu}\frac{\partial p}{\partial x}. \tag{16a}$$

When the macroscopic pressure gradient is parallel to the x axis, inertial effects are neglected and the fluid flow is assumed laminar. More generally, in vectorial terms, this equation is written

$$\boldsymbol{J} = -\frac{\boldsymbol{\sigma}}{\mu} \cdot \overline{\nabla p}. \tag{16b}$$

where $\boldsymbol{\sigma}$ is a 2×2 tensor. In the rest of this paper, the transmissivity is assumed to be a scalar σ (with $\boldsymbol{\sigma} = \sigma \boldsymbol{I}$ where $\boldsymbol{I}$ is the two-dimensional unit tensor). Because of its definition, it is important to note that σ is homogeneous to the cube of a length. More details are given in [10].

The calculations of the fracture transmissivity can be done in different ways. It should be noted that the same codes calculate porous media permeability and fracture transmissivity. This could be addressed in three different ways: namely the classical finite volume technique applied to cubic voxels [23], a Lattice Boltzmann model [12], and the finite volume technique applied to tetrahedra [26]. In this contribution, the second technique is applied since the corresponding code is parallel, and thus significantly faster.

The elementary case of the Poiseuille flow corresponds to a channel limited by two infinite planes separated by a distance b. The resulting velocity profile is parabolic and the transmissivity is given by

$$\sigma = \frac{b^3}{12}. \tag{17}$$

In the following, this simple formula, which accounts for one single crack opening b and no tortuosity of the fluid path, will be used as a comparison with our 3D calculation results.

For the sake of clarity, let us introduce some notations. The cubic voxel size is denoted a (in μm or nm), and its value is given whenever needed. The dimensional permeability is denoted K_{ii} where the subscript i is equal to x, y, or z, depending on the direction along which the calculation is performed. The dimensionless permeability is indicated by a prime and is given by

$$K'_{ii} = \frac{K_{ii}}{a^2}. \tag{18}$$

B. Application to the FIB-SEM sample

The initial data is a block of size $674\times562\times300$ voxels, which is represented in Fig. 6(a). The initial voxels are parallelipipedic (not cubic) and of sides 48.8, 35.71, and 50 nm. In order to minimize boundary effects, the mirror image of this block is taken and the percolating components along the y axis are determined; then, the medium is redefined as a medium made of cubic voxels of side $a = 35.71$ nm. The corresponding medium of size $680\times1124\times420$ voxels is shown in Fig. 6(b). Note the change of shape between (a) and (b), which is due to the change of voxel representation.

There is a horizontal solid region in the upper part of the sample, which crosses the whole sample, and which is attributed to a measurement artifact. This line implies that the permeability along the z axis is zero; hence, calculations are done only along the y axis. A first calculation involves the whole percolating volume, and several subsamples are also calculated for dimensionless permeability.

The dimensionless permeability of the whole percolating component displayed in Fig. 6(b) is equal to

$$K'_{yy} = 0.66\times10^{-3}. \tag{19}$$

A first subsample called sech1 is cut in the percolating component [Fig. 8(a)]. It takes mostly into account the first part of the sample, the one where the crack aperture is almost never equal to 0; it includes a part of the wing which belongs to zone 3 and which is going to be analyzed below; note that this wing percolates by itself along the y axis. Its size (including the mirror image) is $511\times512\times206$ voxels. The corresponding dimensionless permeability is calculated and found to be equal to

$$K'_{yy} = 9.29\times10^{-3}. \tag{20}$$

In order to analyze the influence of the wing in the sample sech1, this wing has been suppressed and the corresponding sample sech11w is displayed in Fig. 8(b). The corresponding dimensionless permeability is calculated and found to be equal to

$$K'_{yy} = 5.25\times10^{-3}. \tag{21}$$

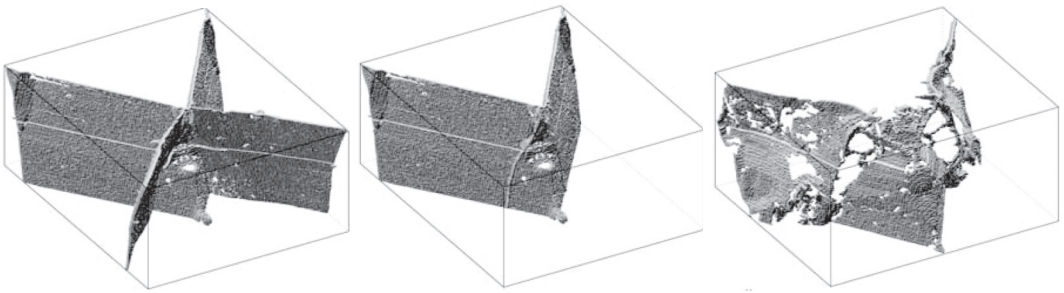

(a) (b) (c)

FIG. 8. Subsamples of the FIB-SEM pore volume sample (displayed in Fig. 6) taken from T-2390-82 sandstone. Zone 1: sech1 (a) and sech11w (b). Zone 2: sech2 (c).

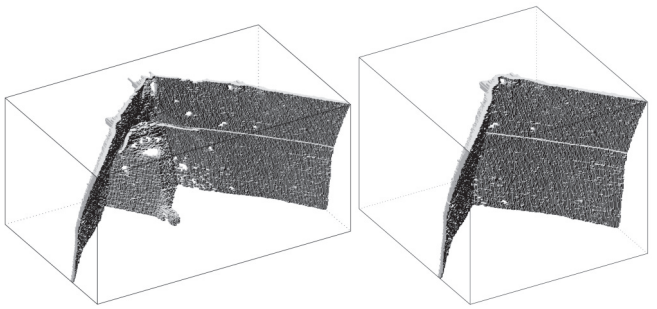

FIG. 9. Subsamples of the FIB-SEM pore volume sample (displayed in Fig. 6) taken from T-2390-82 sandstone: (a) zone 3 with remnants of zone 1 and its mirror image; (b) subsample of the wing and its mirror image along the y axis.

As expected, the permeability decreases since the wing percolates by itself.

A second subsample called sech2 is cut in the sample displayed in Fig. 6. It mostly takes into account the second part of the sample, where the aperture is often equal to 0. It is displayed in Fig. 8(c). Its size is the same as the one of subsample sech1. The corresponding dimensionless permeability is calculated and found to be equal to

$$K'_{yy} = 0.62\times10^{-3}. \tag{22}$$

It is observed that subsample sech2 is about ten times less permeable than sech1. This is logical when the two sample pore volumes (in terms of thickness, tortuosity, volume) are visually compared.

Finally, another region is analyzed in zone 3, as indicated in Fig. 6(b). The wing for large values of x is selected. In order to better locate the fracture, which is calculated, three successive selections are shown in Figs. 9(a)–9(c). The beginning is always the same: we want to get rid of zone 1 which intersects zone 3, as is clear in (a) for instance. This selection is achieved in (c) and the mirror image along the y axis is used to obtain sample (d), on which the calculations are performed. The horizontal solid region mentioned at the beginning of this Subsection appears clearly in these images.

The corresponding dimensionless permeability is calculated and found to be equal to

$$K'_{yy} = 1.16\times10^{-2}. \tag{23}$$

This is the largest permeability obtained in the three well defined zones of the whole FIB-SEM sample. It is greater than that of the whole percolating volume.

C. Application to the CMT rod sample from sample T-2390-82

The analysis is performed on the rod-shaped sample of about 0.946 mm×0.667 mm section and 2 cm height [Fig. 5 (right) and Table I]. The cubic voxel size a is equal to 600 nm.

This sample is processed in the same way as the FIB-SEM one. Its mirror image along the y axis is added and only the percolating component is retained. This analysis allows a reduction of the total useful size of the sample, which is found to be 804×1436×414 voxels. The result is shown in Fig. 10(a).

As previously, three types of calculations are performed, corresponding to the media displayed in Fig. 10: namely the full percolating component (a), a permeable portion (b), and a less permeable portion (c). The corresponding dimensionless permeabilities and sizes (in voxels) are

$$K'_{yy}(a) = 0.175\times10^{-2}, \quad \text{size: } 804\times1436\times414, \tag{24a}$$

$$K'_{yy}(b) = 0.267\times10^{-2}, \quad \text{size: } 534\times576\times414, \tag{24b}$$

$$K'_{yy}(c) = 0.466\times10^{-3}, \quad \text{size: } 270\times576\times414. \tag{24c}$$

The results are in agreement with physical intuition. Indeed, the permeability of portion (b) is five times larger than that of the less permeable portion (c), while the permeability of the whole medium is intermediate.

D. Dimensional transmissivities

Some transformations are needed in order to change the permeabilities of the FIB-SEM and CMT samples to fracture transmissivities σ, which are homogeneous to the cube of a length, and directly comparable from one sample to the other. Let Q be the flow rate through the surface $S = N_{cx}\times N_{cz}a^2$,

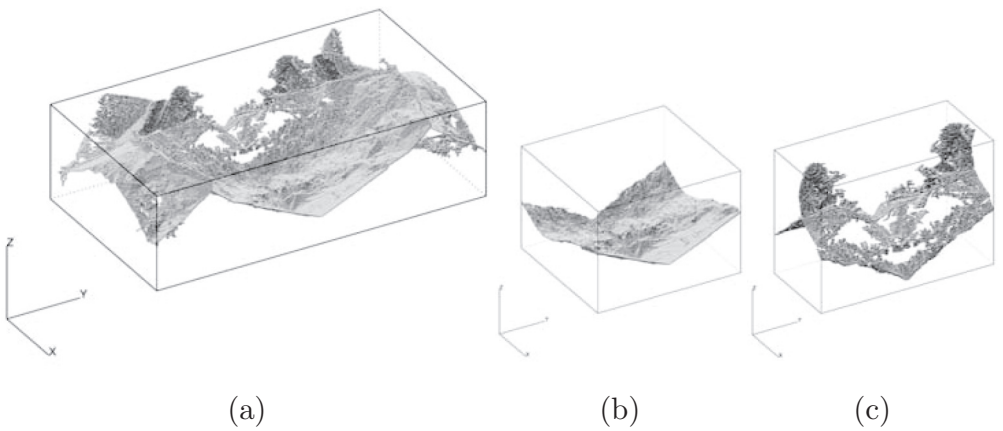

FIG. 10. 3D rendering of the pore volume of the CMT rod-shaped sample taken from T-2390-82 sandstone (see Fig. 5 right). (a) The percolating component of the full sample is completed by its mirror image along the y axis. (b) A permeable central portion of (a). (c) A less permeable central portion of (a).

where N_{cx} and N_{cz} are the total voxel numbers along the x and z axes, respectively. Darcy's law is expressed as

$$\frac{Q}{S} = -\frac{K_{yy}}{\mu}\nabla p. \tag{25a}$$

where μ is the fluid viscosity and p the pressure. Darcy's law for fractures is expressed as

$$\frac{Q}{N_{cz}a} = -\frac{\sigma}{\mu}\nabla p \tag{25b}$$

since for fractures it is the flow rate per unit width of the fracture, which is taken into account. In relations (25), the fracture is assumed to be perpendicular to the xz plane and vertical. As seen in Figs. 6–9, this is not exactly true for the FIB-SEM sample, but the difference is likely to be small.

For the CMT sample, the fracture is horizontal and its width is better approximated by $N_{cx}a$. Therefore, equating the flow rate Q expressed by these relations yields

$$\sigma = N_{cx}aK_{yy} = N_{cx}a^3K'_{yy} \quad \text{(FIB-SEM sample)}, \tag{26a}$$

$$\sigma = N_{cz}aK_{yy} = N_{cz}a^3K'_{yy} \quad \text{(CMT sample)}. \tag{26b}$$

Finally, Table II shows that the fracture transmissivity undergoes large variations, from 1.4×10^{-24} to 2.4×10^{-19} m^3. The two samples have very different fluid flow abilities: the transmissivity of the first one (FIB-SEM) is about 10^{-22} m^3, while the second one (CMT) is about 10^{-19} m^3, i.e., three orders of magnitude greater.

As a matter of comparison, let us use Poiseuille's law for a plane flow between two flat surfaces [Eq. (17)], with the measured peak crack apertures for the FIB-SEM sample (180 nm) and the CMT sample (4 μm). This yields the following fracture transmissivities:

$$\sigma = 4.8\times10^{-22} \quad \text{(FIB-SEM sample)}, \tag{27a}$$

$$\sigma = 5.3\times10^{-18} \quad \text{(CMT sample)}. \tag{27b}$$

When compared to our predictions of transmissivities obtained by solving in 3D the Stokes equation (Table II), these values of σ (given by Poiseuille's law) are very close for the FIB-SEM sample, while they are one order of magnitude greater for the CMT sample.

V. DIMENSIONAL MACROSCOPIC PERMEABILITIES AND DISCUSSION

The estimations of (13) and of Table II are now combined. When the minimal (respectively maximal) estimations of the network permeability K' and of the fracture transmissivities σ are combined, the following range of variations is obtained:

$$0.66\times10^{-24}\times198 < K_n < 2.4\times10^{-19}\times3083$$
$$\Rightarrow 1.3\times10^{-22} < K_n < 7.4\times10^{-16} \tag{28}$$

If the two samples are distinguished, one obtains the following:

For the FIB-SEM sample,

$$0.66\times10^{-24}\times198 < K_n < 2.16\times10^{-22}\times3083$$
$$\Rightarrow 1.3\times10^{-22} < K_n < 6.7\times10^{-19}\ \text{m}^2. \tag{29a}$$

For the CMT sample,

$$4.2\times10^{-20}\times198 < K_n < 2.4\times10^{-19}\times3083$$
$$\Rightarrow 8.3\times10^{-18} < K_n < 7.4\times10^{-16}\ \text{m}^2. \tag{29b}$$

The permeability predicted from 2D SEM and FIB-SEM (0.0085–0.56 nD) is smaller than the actual sandstone permeability (0.014 mD) by about two orders of magnitude.

In contrast, the permeability range predicted with 2D SEM and CMT (0.0083–0.074 mD) corresponds rather well to the actual gas permeability of T-2390-82 sandstone (0.014 ± 0.005 mD). The large range of predictions is related to the significant variability of the pore network identified by 2D SEM. It is noted that the permeability prediction closest to the measured data (7.4×10^{-17} m^2, i.e., 0.074 mD) corresponds to the high crack density zone imaged by 2D SEM. This means that gas passes preferentially through a limited, localized, amount of microcracks, whereas significantly smaller transport occurs through finer porosity. In particular, the permeability through cracks of 180 nm (such as those imaged by FIB-SEM) is two to five orders of magnitude below the macroscopically measured values. It means that gas passes through these parts of the pore network, which represent 1.25% porosity (on a total of 3%), yet with a significantly slower rate than through the cracks providing 0.074 mD.

It is concluded that the low permeability sandstone is characterized by two features, namely the existence of two very different scales (corresponding to the individual microcracks and to their network) and the large variability of the properties of the porous space which is present at all investigated scales.

From this study, it also appears that the proposed methodology is sound and could be extended to other materials. The length scale gap between the smallest and the largest scale is so large that it is at the moment technically impossible to solve directly the Stokes equation in a network of microcracks. The real size of the images in Fig. 3 is on the order of 1 mm; the smallest voxel size used for solving the Stokes equation is equal to 35.7 nm. Therefore, a brute force approach would require a sample, which linear size would be equal to 10^5 voxels. Presently, the size of the largest arrays, which are tackled, is smaller than 10^4 voxels. Therefore, the ratio between the actual possibilities and what would be required is of 10, but the ratio of the full three dimensional sizes is 1000, which is obviously out of our reach for some time. It might be of interest to recall that the first calculations for a cell size of $N_c = 27$ were performed at the beginning of the 1990s [23], and that calculations for $N_c = 1000$ have been routinely done for ten years. The proposed double-step methodology seems the only one feasible for the next few years.

The large variability of the properties of the porous space poses a similar problem. The FIB-SEM yields detailed and local views of microcracks. The CMT can image an individual microcrack with a voxel size of 0.6 μm, and this crack is at a different scale than that imaged by FIB-SEM (voxel size on the order of 35–50 nm).

The brute force approach would consist of rediscretizing the previous block by a series of blocks with a voxel size on the order of 35 nm. This would require us to take 40^3 such local measurements, which seems again out of reach at the moment. Given that permeability is mainly controlled by cracks on

the order of 1 μm, this may not be the wisest approach. Similarly, characterizing the crack opening distribution b from SEM observations, as in Fig. 4, would require to image and compute several hundreds of images for proper statistical representativeness. This is a heavy task, which would lead to a biased distribution of b, as it is measured in 2D (and not in 3D). It is why this approach has not been privileged in this contribution.

VI. CONCLUDING REMARKS

For tight sandstone T-2390-82, the relevant pore structure for fluid transport is well described on two separate scales; the microcrack network is imaged and characterized by 2D SEM; the individual crack between quartz grains is characterized on a 350 nm scale by MIP, which is of the same order of magnitude as the 180 nm opening given by FIB-SEM. This crack scale contributes by four orders of magnitude less to transport than the micrometric fissure aperture obtained by CMT (of 4 μm wide). The latter provides macroscopic permeability prediction consistent with gas permeability identification on centimetric samples.

However, it should be mentioned that the smallest cracks may prove important for other processes such as dispersion and two-phase flow.

Two important remarks can still be made regarding the permeability prediction at the scale of the fracture network. Probably, the data corresponding to the number of intersections per unit length is the most precise. There is no ambiguity, as in the two other methods, where fracture and intersection counting are much more subjective. Other quantities could be used such as the fracture length per unit surface, as detailed in [10].

Finally, the two scale methodology is not definitely demonstrated by this single application. The purpose of this work was to demonstrate its feasibility and to give some hints on its validity. Therefore, this original approach still needs to be validated on other tight sandstones to prove its generality.

ACKNOWLEDGMENTS

Financial support by GDF/Suez E&P is gratefully acknowledged. The SEM national facility available at the Centre Commun de Microscopie de Lille (France) is supported by the Conseil Regional du Nord-Pas de Calais, and by the European Regional Development Fund (ERDF). Part of this work was performed when P.M.A. was supported at the Mechanical Engineering Department, Technion, Haifa, Israel by a fellowship of the Lady Davis Foundation.

APPENDIX: EXPERIMENTAL METHODS AND IMAGE PROCESSING TECHNIQUES

1. X-ray romputed microtomography (CMT)

The CMT scan is made in an Ultratom device at a voxel size of 0.6 μm with the following setup: (1) Hamamatsu nanofocus x-ray tube equipped with a LaB_6 filament and a 1 μm thickness tungsten target, thus providing a spot size of 0.25 μm for x-ray emission and (2) a 4000×2624 pixels CCD camera combined with a Gadox scintillator used in binning 2×2 for a better signal-to-noise ratio. The resulting physical pixel size is 23.6 μm. The experimental settings are chosen to enhance projection contrast while preserving an acceptable scan duration of less than 3 h; see Table III. After the reconstruction procedure and acquisition artifacts removal, an output volume of $1578\times1113\times1262$ voxels, linearly scaled into a 16 bit format, is computed.

From these images, we have extracted the pore network in 3D. To do so, we have selected 500 images in order to retain only those presenting visible porosities (resembling joints or cracks). Segmentation is performed to extract the pores (in black) with respect to the solids (in white). Binary images are plotted in 3D by a surface rendering process (AMIRA software, FEI). The image processing technique is as follows.

After automatic thresholding (i.e., segmentation) by each of the 17 available algorithms in the IMAGEJ software, the images consistently display non-negligible "salt-and-pepper" noise (small amounts of pixels evenly distributed and without clear relation to the actual microstructure). The Isodata algorithm in IMAGEJ allows us to recognize reliably large cracks (or joints) between SiO_2 grains, yet it also retains significant salt-and-pepper noise. No better result is obtained with other algorithms. Even though salt and pepper noise is easily removed by 2D or 3D median filters, the latter will also remove a great part of the cracks, which are often less than 10 pixels wide. Hence, 2D or 3D median filters are not used. Another method is applied, which preserves the original cracks.

Our method consists of overlapping (1) the images segmented with the Isodata algorithm and (2) enlarged crack profiles. The latter are used as a mask to preserve the cracks when subtracting the salt-and-pepper noise. Enlarged crack profiles are obtained on the original grayscale images by selecting manually as many connected cracks as possible in all slices (3D), with the magic wand tool available in FEI AMIRA; while doing so, we neglect all noise (i.e., all clusters of dark pixels smaller than 5). With this method, selected cracks are of much narrower width than those obtained after segmentation by the Isodata algorithm, and they cannot be used as crack profiles. Hence, the selected cracks are processed with the Dilation tool in IMAGEJ, with an Iteration parameter of 3 and a Count of 1.

TABLE III. Experimental settings for x-ray computed microtomography (XCMT).

Acceleration voltage U (kV)	Filament intensity I (μA)	Voxel Size (μm)	Number of projections over a turn	CCD exposition time (s)	Number of averaged radiographies
80	94	0.6	1600	0.85	8

Then, we use the "Process > Image Calculator > option: AND" tool in IMAGEJ, on the binary images obtained after using the Isodata algorithm and with the dilated cracks used as a mask.

Finally, all images are computed with the tool Process-Binary-Open (Iteration of 3 and Count of 5) in IMAGEJ to soften the crack edges. A number of other algorithms has been attempted, but, among all our tests, this is what is closest to the original images.

2. FIB-SEM

For FIB-SEM imaging, the sample is finely polished (down to mirrorlike finish). The focused ion beam (FIB) cuts a U-shaped hole in order to isolate a plane-parallel sandstone volume [27]. The plane-parallel sandstone volume is then covered with a platinum coating, in order to provide adequate electrical conductivity to the sample. This also allows maximum contrast with the observed surface. Following this, the FIB cuts regularly-spaced 50 nm thick slices from the plane-parallel volume, perpendicular to the sample polished surface. Between each FIB cutting, the sandstone matter perpendicular to the polished surface is observed with an electron detector of the *in lens* type, which detects both secondary and backscattered electrons. This provides an image reflecting both the sample roughness (thanks to the SE) and its chemical composition (the image contrast is given by the BSE). Four stacks of 300 images were taken of the T-2390-82 sandstone sample. Currently, only one has been computed to provide a 3D pore network (image series no. 110331-Gres-239082-Serie03); see Fig. 6.

Computation mainly consists of tilting the images in order to account for the 52° angle of the electron beam with respect to the imaged plane, aligning and cropping the images to select successive areas, removing the background, removing vertical artifacts (with a fast Fourier transform), using the Median Filter 3D with a 1.5 pixel size (to remove salt-and-pepper effects), normalizing the histograms of all images, and, finally, segmenting (thresholding) the images. After such process, pores appear black and solids appear white. This image processing is performed by using the free software IMAGE J. Each of the 17 available segmentation algorithms has been tested, and the corresponding porosities were plotted. While 12 algorithms provide unrealistic porosities (above 50%)—i.e., too dark images after segmentation—three of them provide very close porosities: 1.31% with MaxEntropy, 1.25% with RenyiEntropy and 1.25% with the Yen algorithm; the Shanbhog algorithm alone provides 5.37% porosity, which is visually excessive. All three similar porosities of 1.25–1.31% are realistic when compared to other porosity measurement means, and they are visually consistent with the original images. In all further pore analyses, segmented images using the Yen algorithm were chosen.

[1] K. W. Shanley, R. M. Cluff, and J. W. Robinson, AAPG Bull. **88**, 1083 (2004).

[2] J. Kamath, R. E. Boyer, and F. M. Nakagawa, SPE Formation Eval. **7**, 219 (1992).

[3] B. F. Swanson, J. Petrol. Technol. **33**, 2498 (1981).

[4] J. H. M. Thomeer, J. Petrol. Technol. **12**, 73 (1960).

[5] J. H. M. Thomeer, J. Petrol. Technol. **35**, 809 (1983).

[6] X. Fu, Ph.D. thesis in Civil Engineering (in French), Ecole Centrale de Lille, 2013.

[7] Z. Duan, C. A. Davy, F. Agostini, and F. Skoczylas, Int. J. Rock Mech. Min. **65**, 75 (2014).

[8] Y. Song, C. A. Davy, D. Troadec, A.-M. Blanchenet, F. Skoczylas, J. Talandier, and J.-C. Robinet, Mar. Petrol. Geol. **65**, 63 (2015).

[9] P. Adler and J.-F. Thovert, *Fractures and Fracture Networks* (Kluwer, Dordrecht, 1999).

[10] P. Adler, J.-F. Thovert, and V. Mourzenko, *Fractured Porous Media* (Oxford University Press, Oxford, 2012).

[11] V. V. Mourzenko, J.-F. Thovert, and P. M. Adler, Phys. Rev. E **84**, 036307 (2011).

[12] A. Pazdniakou and P. M. Adler, Adv. Water Resour. **62**, 292 (2013).

[13] C. A. Davy, F. Skoczylas, J.-D. Barnichon, and P. Lebon, Phys. Chem. Earth **32**, 667 (2007).

[14] J. Rouquerol, D. Avnir, C. W. Fairbridge, D. H. Everett, J. M. Haynes, N. Pernicone, J. D. F. Ramsay, K. S. W. Sing, and K. K. Unger, Pure Appl. Chem. **66**, 1739 (1994).

[15] D. N. Dewhurst, R. M. Jones, and M. D. Raven, Petrol. Geosci. **8**, 371 (2002).

[16] Y. Song, C. A. Davy, P. Bertier, and D. Troadec, Micropor. Mesopor. Mater. **228**, 64 (2016).

[17] G. Peix, P. Duvauchelle, and N. Freud, in *X-Ray Tomography in Material Science* (Hermes Science, London, 2000), Chap. 1, pp. 15–27.

[18] A. C. Kak and M. Slaney, *Principles of Computerized Tomographic Imaging* (IEEE Press, Piscataway, NJ, 1988).

[19] B. Munch and L. Holzer, J. Am. Ceram. Soc. **91**, 4059 (2008).

[20] L. M. Keller, L. Holzer, R. Wepf, and P. Gasser, Appl. Clay Sci. **52**, 85 (2011).

[21] L. M. Keller, Ph. Schuetz, R. Erni, M. D. Rossell, F. Lucas, M. Lucas, Ph. Gasser, and L. Holzer, Micropor. Mesopor. Mater. **170**, 83 (2013).

[22] L. M. Keller, L. Holzer, Ph. Schuetz, and P. Gasser, J. Geophys. Res., Solid Earth **118**, 2799 (2013).

[23] P. M. Adler, C. G. Jacquin, and J. A. Quiblier, Int. J. Multiphase Flow **16**, 691 (1990).

[24] P. Spanne, J.-F. Thovert, C. J. Jacquin, W. B. Lindquist, K. W. Jones, and P. M. Adler, Phys. Rev. Lett. **73**, 2001 (1994).

[25] V. V. Mourzenko, J.-F. Thovert, and P. M. Adler, J. Phys. II **5**, 465 (1995).

[26] I. Malinouskaya, V. V Mourzenko, J.-F. Thovert, and P. M. Adler, Phys. Rev. E **77**, 066302 (2008).

[27] L. Holzer, F. Indutnyi, P. Gasser, B. Munch, and M. Wegmann, J. Microsc. **216**, 84 (2004).